Journal of Solid State Chemistry 181 (2008) 2549–2558

Contents lists available at ScienceDirect

Journal of Solid State Chemistry

journal homepage: www.elsevier.com/locate/jssc

Next-nearest neighbour contributions to the XPS binding energies and XANES absorption energies of P and As in transition-metal arsenide phosphides $MAs_{1-y}P_y$ having the MnP-type structure

Andrew P. Grosvenor, Ronald G. Cavell, Arthur Mar *

Department of Chemistry, University of Alberta, Edmonton, Alberta, Canada T6G 2G2

ARTICLE INFO

Article history:
Received 20 December 2007
Received in revised form
11 June 2008
Accepted 12 June 2008
Available online 19 June 2008

Keywords:
XPS
XANES
Next-nearest neighbour shift
Charge potential model
Phosphides
Arsenides

ABSTRACT

X-ray photoelectron spectroscopic (XPS) and X-ray absorption near-edge spectroscopic (XANES) measurements have been made for several series of metal arsenide phosphides $MAs_{1-y}P_y$ (M = Co, Fe, Cr) that adopt the MnP-type structure. The P and As XPS binding energies (BEs) and XANES absorption energies of the metal arsenide phosphides do not follow the trend observed for the simple binary phosphides or arsenides, a deviation that arises from the combination of nearest and next-nearest neighbour contributions acting on the P or As photoemission or absorption site. The P $2p_{3/2}$ BEs and K-edge absorption energies are lower in $MAs_{1-y}P_y$ than in MP because the P atoms are more negatively charged and because the P photoemission or absorption site is screened to a greater extent by less positively charged nearest-neighbour M atoms and more negatively charged next-nearest neighbour P atoms. The As L_3- and K-edge absorption energies are higher in $MAs_{1-y}P_y$ than in MAs primarily because the As atoms are less negatively charged. The M charge has been evaluated from analysis of the M 2p XPS spectra and the M L- and K-edge XANES spectra.

1. Introduction

Although X-ray photoelectron spectroscopy (XPS) is frequently applied to examine surfaces, it is well established that XPS can also provide information about the electronic structure of bulk solids through analysis of line shapes and binding energies (BE). A charge potential model has been developed to describe BE shifts in terms of ground-state effects [1–3]:

$$\Delta E = E_i - E_i^0 = k\Delta q_i + \Delta \sum_{j \neq i}^{n} q_j / r_{ij} \quad (1)$$

Within different compounds, an atom i acquires a BE (E_i) that is shifted relative to a reference energy E_i^0 because of variations in two possible factors: (i) the atomic charge (q_i in $k\Delta q_i$, where k is a constant representing interactions between valence and core electrons), and (ii) the chemical environment ($\Delta\Sigma_{j\neq i}\ q_j/r_{ij}$), where r_{ij} is the distance to neighbouring atoms j [1,2]. The second term, often called the Madelung or crystal potential because of its equivalence to the same concept in ionic solids, describes how the charges of coordinating atoms, q_j, surrounding the photoemission site influence the BE of the resulting photoelectron [1,4]. Effectively, how well the nuclear charge is screened within the atom of interest depends on the magnitudes of these intraatomic ($k\Delta q_i$) and interatomic ($\Delta\Sigma_{j\neq i}\ q_j/r_{ij}$) terms, the latter usually playing a less significant role. Although the immediate coordination environment (the nearest neighbours around an atom) constitutes the most important contribution to the interatomic term, the more extended environment (the *next*-nearest neighbours) may also affect the BEs, albeit to a lesser extent. For example, when H is substituted by F in polymers, the α-C atom (bound directly to F) experiences an increase in the C 1s BE of ~3 eV because it becomes more positively charged and thus the magnitude of the intraatomic term is increased [5]. The β-C atom (bound to the α-C) also experiences a positive, but smaller, shift in BE of ~1 eV because the Madelung potential it feels is modified by the new charge on the α-C [5]. Accordingly, this effect is called a next-nearest neighbour (β- or secondary substituent) shift [6]. In addition to ground-state effects, after a photoelectron is ejected, the production of a core hole causes electrons to relax towards the atom, modifying the final-state energy and thereby the photoelectron BE [6]. These final-state effects can be added to the ground-state effects described by Eq. (1) through additional terms, $-(\Delta E_i^{IA1}+\Delta E_i^{IA2})$, that represent intraatomic (IA1) and interatomic (IA2) relaxation, the former usually being negligible [6].

The electronic structure of solids can also be analysed by X-ray absorption spectroscopy, which can be subdivided into X-ray

* Corresponding author. Fax: +1 780 492 8231.
E-mail address: arthur.mar@ualberta.ca (A. Mar).

0022-4596/$ - see front matter © 2008 Elsevier Inc. All rights reserved.
doi:10.1016/j.jssc.2008.06.034

absorption near-edge spectroscopy (XANES) and extended X-ray absorption fine structure (EXAFS) [7,8]. XANES probes the absorption edge wherein core electrons are excited into bound or continuum states, thereby giving information about atomic charge and coordination environment [8]. EXAFS results from constructive and destructive interference of photoelectrons that are backscattered by atoms surrounding the absorption site (in the case of single scattering); oscillations are observed in the absorption spectrum, often at energies well above the absorption edge. Analysis of these oscillations gives information about the local structure surrounding the absorbing atom [7]. EXAFS oscillations superimposed near the absorption edge often render quantitative analysis of XANES spectra difficult. As is the case for XPS BEs, X-ray absorption threshold energies depend on similar factors to those described by Eq. (1) [9]. However, because electrons are now promoted into bound or continuum states, they will still provide partial screening to the excited atom. This implies that absorption energies are less sensitive to relaxation effects than are XPS BEs. For example, in the series of compounds MnO, $LaMnO_3$, and $CaMnO_3$, the calculated Mn K-edge absorption threshold energies increase as the occupancy of the Mn 3*d* band and the Madelung potential change [9]. The shifts in these Mn K-edge absorption energies are much larger than the shifts in the Mn 1*s* XPS BEs because the absorption energies are not dampened by relaxation effects [9]. Next-nearest neighbour effects have also been identified in XANES [10].

Recently we have used XPS and XANES to examine binary and pseudobinary transition-metal phosphides *M*P and $M_{1-x}M'_xP$, the majority of which possess the MnP-type structure [11,12]. These materials are of interest because of their magnetic properties and catalytic activity [13,14]. The structure consists of an arrangement of metal-centred distorted octahedra (Fig. 1), which form networks of strong metal–metal and weak P–P bonds [15], consistent with the charge formulation $M^{1+}P^{1-}$ [11]. Compounds of this structure type are metallic [13]. Throughout the series of binary phosphides *M*P, the P $2p_{3/2}$ XPS BEs and P K-edge absorption energies decrease linearly as the difference in electronegativity between *M* and P increases as we progress from CoP to CrP (all MnP-type), to VP (NiAs-type), and finally to TiP (TiAs-type) [12]. As implied by Eq. (1), these shifts arise because as *M* becomes more electropositive, P becomes more negatively charged [12]. In contrast, in the pseudobinary phosphides $M_{1-x}M'_xP$, the P XPS BEs and absorption energies do not follow this linear trend and the shifts are lower than expected. Here, the presence of two different metals interacting through the metal–metal bonding network induces a charge redistribution, the more electropositive metal *M*′ donating electron density not only to P but also to the more electronegative metal *M* [12]. This next-nearest neighbour effect reduces the Madelung potential operating on the P photoemission or absorption site, lowering its energy, especially when the concentration of the more electronegative metal *M* is high [12].

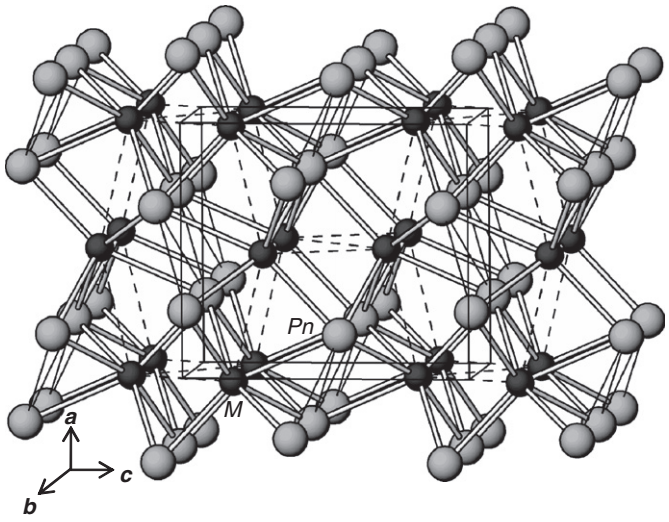

Fig. 1. MnP-type crystal structure viewed down the *b*-axis. The small dark spheres are *M* atoms and the large lightly shaded spheres are *Pn* atoms. The thin dashed lines indicate the *M*–*M* bonding network whereas the thin solid lines indicate the *Pn*–*Pn* bonding network.

Because the next-nearest neighbour effect has been demonstrated to be important in mixed-metal phosphides, it is of interest to determine if it also applies to mixed-anion systems. Several metal arsenide phosphide series $MAs_{1-y}P_y$ with the MnP-type structure are known, wherein As and P atoms are randomly distributed within the anion sites [16,17]. Here we report XPS and XANES spectra of $CrAs_{1-y}P_y$, $FeAs_{1-y}P_y$, and the new series $CoAs_{1-y}P_y$ and apply the charge potential model (Eq. (1)) to explain shifts in their P 2*p* XPS BEs and P K-edge and As L_3- and K-edge absorption energies. The metal 2*p* XPS and L- and K-edge absorption spectra are also presented.

2. Experimental

2.1. Synthesis

Starting materials were metal powders (Cr, 99.8%, Alfa-Aesar; Fe, 99.9%, Cerac; Co, 99.8%, Cerac; V, 99.5%, Alfa-Aesar), red P powder (99%, Alfa-Aesar), and ground As pieces (99.9998%, Alfa Inorganics). Products were identified by their powder X-ray diffraction (XRD) patterns collected on an Inel powder diffractometer equipped with a CPS 120 detector. All samples were stored in a glove box under Ar to limit exposure to air.

Binary monopnictides (CrP, FeP, CoP; CrAs, FeAs, CoAs, VAs) were prepared through stoichiometric reaction of *M* with P or As in sealed and evacuated fused-silica tubes. The tubes were heated to 1323 K (for *M*P) or 1073 K (for *M*As) over 2 days and held at this temperature for at least 5 days before being quenched in water. For *M*As, addition of small amounts of I_2 (Anachemia) improved crystallinity of the products. Ternary pnictides $MAs_{1-y}P_y$ (M = Cr, Fe, Co; $y = 0.10, 0.25, 0.50, 0.75, 0.90$) were prepared through stoichiometric reaction of $(1-y)$ *M*As and y *M*P in sealed and evacuated fused-silica tubes. The tubes were heated to 1173 K over 24 h and held at this temperature for 5 days before being quenched in water. To improve homogeneity, the samples were reground under Ar, resealed in fused-silica tubes, and reheated with the same heating profile; this procedure was repeated over three ($FeAs_{1-y}P_y$, $CoAs_{1-y}P_y$) or four ($CrAs_{1-y}P_y$) cycles. Powder XRD confirmed that all samples were single-phase and had adopted the MnP-type structure. Cell parameters for $CrAs_{1-y}P_y$ and $FeAs_{1-y}P_y$ agree with literature values [16,17], and those for the new series $CoAs_{1-y}P_y$ interpolate smoothly from the end members (Fig. 2), in accordance with Vegard's law [18].

2.2. XPS analysis

Measurements were performed on a Kratos AXIS 165 spectrometer using monochromatic Al $K\alpha$ X-rays. The resolution function for this instrument with this X-ray source was determined from analysis of the Fermi edge of cobalt metal (which is a component in many of the samples studied here) to be 0.4 eV, and the BEs are significant to two decimal places [11,12]. Samples were finely ground under Ar, pressed firmly onto In foil (Alfa-Aesar), and mounted on a Cu sample holder. (The grinding allows samples to be more easily pressed onto the In foil with a flatter surface, which

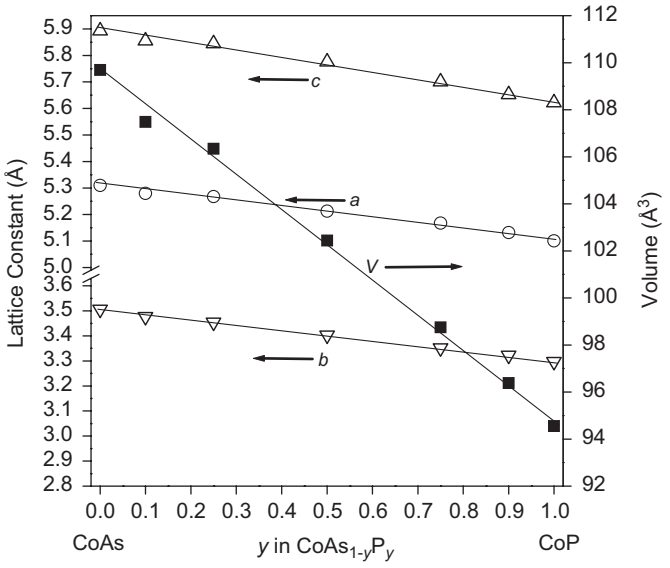

Fig. 2. Plot of orthorhombic cell parameters vs y for the $CoAs_{1-y}P_y$ series, which adopts the MnP-type structure.

is advantageous for the XPS analysis and for ensuring electrical contact.) They were transported and inserted into the introduction chamber of the spectrometer under Ar to reduce the possibility of extensive surface oxidation. Samples were sputter-cleaned *in situ* with an Ar^+ ion beam (4 kV, 10 mA) to remove any surface oxides or contaminants (e.g. C, I) formed. This sputtering process causes slight reduction of As, manifested by a low-BE shoulder in the As 3*d* spectrum, but no effects were observed in the P or *M* spectra. Annealing the samples in vacuum using temperatures as high as 700 K for ~30 min or lowering the Ar^+ ion sputtering current (1 mA) did not eliminate this As reduction. Survey spectra revealed that preferential sputtering of light elements did not occur and that the surface and bulk compositions are similar. For example, different batches of $FeAs_{0.10}P_{0.90}$ (nominal) had a composition of $FeAs_{0.1(1)}P_{1.0(1)}$. High-resolution spectra of the *M* 2*p*, P 2*p*, As 3*d*, and C 1*s* core lines were collected with a pass energy of 20 eV, a step size of 0.05 eV, a sweep time of 180 s, and an energy envelope of 20–40 eV. Spectra were analysed with the aid of the CasaXPS software program [19]. During data analysis, the samples were calibrated using the C 1*s* line arising from adventitious C with a fixed value of 284.80 eV, although this was rarely required because the samples studied are metallic. To remove the background arising from energy loss, a Shirley-type function was applied.

2.3. P K-edge, As L-edge, and M L-edge XANES analysis

P K-, As, L-, and *M* L-edge XANES spectra were collected at the Canadian Light Source (CLS), Saskatoon, Saskatchewan, using the spherical grating monochromator undulator beamline, 11-ID.1 [20]. The flux is ~10^9 photons/s at energies near the P K-edge (~2150 eV) and increases to ~10^{11} photons/s below this energy (1900 eV). The estimated resolution is ~1 eV and a beam size of approximately $50 \times 100\,\mu m$ was used. Powdered samples were mounted on carbon tape and inserted in the vacuum chamber via a load lock. Total electron yield and X-ray fluorescence yield spectra were measured from 30 to 10 eV below the edge to ~35 eV (P), 50 eV (*M*), or 75 eV (As) above the edge at 0.1 eV per step. The P K-edge spectra were calibrated against a sample of $Na_4P_2O_7$, with the peak maximum of the P K-edge set to 2152.4 eV [21]. The As L-edge spectra were calibrated against a sample of Ge with the first derivative of the L_3 edge set to 1217 eV. The *M* L-edge spectra were calibrated against the first derivative of the L_3 edge of the corresponding pure metal with energies of 574.1 eV (Cr), 706.8 eV (Fe), and 778.1 eV (Co). The absorption edge values reported herein represent the maximum of the first derivative peak, to remove the influence of surface phosphates or arsenates formed. A precision of ± 0.1 eV was estimated through comparison of multiple analyses of the compounds studied.

2.4. As K- and M K-edge XANES analysis

XANES spectra of the As and *M* K-edges were collected at Pacific Northwest Consortium/X-ray Operations and Research Collaborative Access Team (PNC/XOR-CAT), Sector 20 at the Advanced Photon Source (APS), Argonne National Laboratory with the bending magnet (20BM) beamline. A silicon (111) double crystal monochromator was used to provide a monochromatic photon flux of ~10^{11} photons/s, with a resolution of 1.4 eV at 10 keV and a beam size of approximately 1×4.5 mm. Finely ground samples were sandwiched between Kapton tape, and positioned 45° to the X-ray beam. The fluorescence spectra were measured with a Canberra 13-element fluorescence detector and transmission spectra were measured with N_2-filled ionization chambers (the I_0 ionization chamber contained a 50:50 mixture of He and N_2). Through the absorption edge, the X-ray energy was increased by 0.15 eV per step. For the *M* K-edge spectra, a standard of the elemental metal was positioned behind the sample and analysed concurrently in transmission mode with N_2-filled ionization chambers, and the peak maximum of the first derivative was calibrated to the accepted values of 5989 eV (Cr), 7112 eV (Fe), or 7709 eV (Co). The As K-edge spectra were calibrated by collecting the Au L_3 spectrum and setting the first derivative to 11919 eV. The precision of the measurements was estimated to be ± 0.1 eV based on multiple analyses of the compounds and the absorption energies reported herein represent the maximum of the first derivative peak. All XANES spectra were analysed using the Athena software program [22].

2.5. Band structure calculations

To interpret the As and *M* K-edge XANES spectra, tight-binding linear muffin-tin orbital band structure calculations were performed on FeAs and $FeAs_{0.50}P_{0.50}$ within the atomic spheres approximation (TB-LMTO ASA) [23]. Contributions from the Fe 4*p*, Fe 3*d*, As 4*p*, and P 3*p* orbitals to the density of states were extracted. Although FeAs and $FeAs_{0.50}P_{0.50}$ adopt the MnP-type structure (space group *Pnma* (no. 62)), mixed occupancy of the As and P atoms in the latter is difficult to treat. Instead, an ordered model of $FeAs_{0.50}P_{0.50}$ was considered, with reduced symmetry in space group $Pcm2_1$ (no. 26). Such a model emphasizes heteroatomic P–As bonds which would be more prevalent in the heavily mixed members of the $FeAs_{1-y}P_y$ series, in contrast to the predominantly homoatomic As–As bonds which would be present in the As-richer members, for which the FeAs band structure would be more appropriate. The calculations were performed with 432*k*-points in the irreducible portion of the Brillouin zone.

3. Results

3.1. Is As less electronegative than P?

In this report, electronegativity differences are identified as a major factor influencing the shifts in energy and variations in

lineshape in the spectra of *M*P, $MAs_{1-y}P_y$, and *M*As. However, the relative electronegativities of P and As on different electronegativity scales are inconsistent (cf., Allred–Rochow, $\chi_P = 2.06$, $\chi_{As} = 2.20$ vs Pauling, $\chi_P = 2.2$, $\chi_{As} = 2.1$) [24–26]. In previous work [11,12], we have preferred to use Allred–Rochow electronegativities because they are derived from atomic properties and thus more closely linked to binding and absorption energies, instead of Pauling electronegativities, which are derived from thermodynamic data [25,26]. Alternatively, we can examine the experimental XPS BE values to determine the electronegativity of As. For example, the skutterudites $CoPn_3$ are known for *Pn* = P, As, Sb, and Co XPS spectra have been measured for CoP_3 and $CoSb_3$ [27]. The Co $2p_{3/2}$ BE decreases from 778.5 eV in CoP_3 to 778.1 eV in $CoSb_3$ because the more covalent character in the Co–Sb bonds leads to better screening of the Co nuclear charge [27]. We have prepared $CoAs_3$ (in a similar manner as CoP_3 and $CoSb_3$) and found that the Co $2p_{3/2}$ BE is 778.3 eV, between those of CoP_3 and $CoSb_3$. This implies that the electronegativity of As is intermediate between P and Sb. If Allred–Rochow electronegativities are chosen for Co ($\chi = 1.70$), P, and Sb ($\chi = 1.82$) and if the Co $2p_{3/2}$ BE shifts are assumed to be linearly proportional to the difference in electronegativity in the Co–*Pn* bond ($\Delta\chi = \chi_{Pn} - \chi_{Co}$), then a revised value of $\chi_{As} = 1.94$ (vs 2.20 as above) is obtained. The interpretation of spectra in the $MAs_{1-y}P_y$ compounds below will thus be based on this revised value, which makes As less electronegative than P.

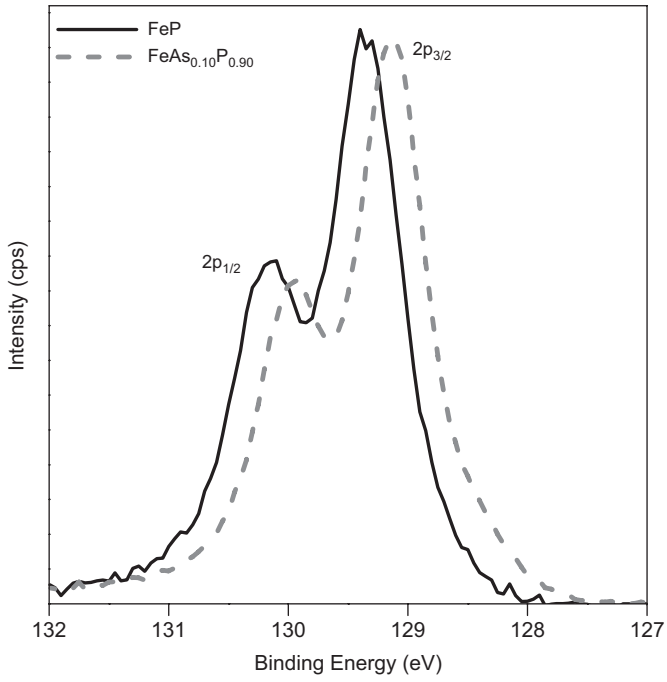

Fig. 3. High-resolution P 2*p* XPS spectra for FeP and $FeAs_{0.10}P_{0.90}$, with $2p_{3/2}$ and $2p_{1/2}$ component peaks labelled. The FeP spectrum, which was measured by the authors of this work on a similar instrument, is taken from Ref. [11].

3.2. P 2p XPS and P K-edge XANES spectra

The spectra of FeP and $FeAs_{0.10}P_{0.90}$ (Fig. 3) reveal a distinct separation between the $2p_{3/2}$ and $2p_{1/2}$ spin–orbit coupled final states, which can be fitted by component peaks having a full-width at half-maximum of ~0.7–0.8 eV with an intensity ratio of 2:1 ($2p_{3/2}$:$2p_{1/2}$), equal to the theoretical value [6]. In the mixed-metal phosphides $M_{1-x}M'_xP$ examined previously, the component peaks were much broader than those in the binary phosphides because different local distributions of *M* and *M*′ atoms are present in the first coordination shell around the P photoemission site [12]. No such broadening is observed in $FeAs_{0.10}P_{0.90}$ relative to FeP, probably because the different local distributions of P and As atoms in the second coordination shell around the P photoemission site are further away.

Table 1 lists P $2p_{3/2}$ BEs for various *M*P and $MAs_{1-y}P_y$ compounds. From multiple measurements on separately synthesized samples or of the same sample examined at different times, we deduce that the precision of these BEs is better than ±0.10 eV

Table 1
P $2p_{3/2}$ and *M* $2p_{3/2}$ XPS binding energies (eV) and P K-, As L_3-, and As K-edge absorption energies (eV) in *M*P, $MAs_{1-y}P_y$, and *M*As

Compound	P $2p_{3/2}$ BE	P K-edge	As L_3-edge	As K-edge[a]	Co $2p_{3/2}$ BE	Fe $2p_{3/2}$ BE	Cr $2p_{3/2}$ BE
CoP	129.49[b]	2142.9[c]			778.33[b]		
FeP	129.34[b]	2142.8[c]				706.91[b]	
MnP	129.18[b]	2142.6[c]					
CrP	129.11[b]	2142.5[c]					573.87[b]
VP	128.82[c]	2142.1[c]					
TiP	128.51[c]	2141.7[c]					
CoAs			1322.1	11866.7	777.91		
FeAs			1322.0	11866.6		706.66	
CrAs			1321.7	11866.4			573.80
VAs			1321.5				
$CoAs_{0.10}P_{0.90}$	129.34	2142.7	1322.4	11866.9	778.22		
$CoAs_{0.25}P_{0.75}$	129.35	2142.7	1322.3	11866.9	778.20		
$CoAs_{0.50}P_{0.50}$	129.39	2142.8	1322.2	11866.9	778.16		
$CoAs_{0.75}P_{0.25}$	129.40	2142.9	1322.1	11866.7	778.11		
$FeAs_{0.10}P_{0.90}$	129.20	2142.6	1322.2	11866.9		706.81	
$FeAs_{0.25}P_{0.75}$	129.24	2142.6	1322.2	11866.8		706.85	
$FeAs_{0.50}P_{0.50}$	129.24	2142.7	1322.1	11866.6		706.77	
$FeAs_{0.75}P_{0.25}$	129.28			11866.6		706.76	
$FeAs_{0.90}P_{0.10}$	129.33			11866.6		706.76	
$CrAs_{0.10}P_{0.90}$	128.99	2142.4	1322.0	11867.1			573.81
$CrAs_{0.75}P_{0.25}$	129.06	2142.4	1321.8	11867.0			573.90

[a] Because the As K-edge absorption threshold energy is overlapped by the intense pre-edge peak and EXAFS peaks, as described in Section 3.3, caution must be applied when interpreting these values.
[b] Ref. [11].
[c] Ref. [12].

(Table S1 in Supplementary Data). Fig. 4a shows a plot of BE vs difference in electronegativity ($\Delta\chi = \chi_P - \chi_M$). Although the P $2p_{3/2}$ BEs decrease linearly through the binary phosphide *M*P series from CoP to TiP, as discussed previously [12], they do not follow this trend in the mixed pnictides $MAs_{1-y}P_y$, with the BEs being lower than expected. Within a given $MAs_{1-y}P_y$ series, the P $2p_{3/2}$ BEs actually deviate more with *increasing* P concentration. Table 1 also lists P K-edge absorption energies from XANES, a bulk-sensitive technique. A representative P K-edge spectrum for $CoAs_{0.10}P_{0.90}$ is shown in Fig. 5a. A similar behaviour to that observed by analysis of the P $2p$ BEs is revealed in a plot of P K-edge absorption energies vs $\Delta\chi$ (Fig. 4b), confirming that these shifts arise from a bulk rather than a surface electronic effect.

3.3. As L- and K-edge XANES spectra

Although As 3*d* XPS spectra were also collected, their analysis was complicated by the presence of a low-BE shoulder (arising from slight reduction of As atoms during Ar^+ ion sputtering, as noted in Section 2.2) and by the partial overlap with Cr 3*p* signals in CrAs and $CrAs_{1-y}P_y$. To circumvent these difficulties, As L- and K-edge XANES spectra were investigated. A representative As L_3-edge spectrum for CrAs, resulting from excitation of As $2p$ electrons into either As 4*s* or 4*d* states, is shown in Fig. 5b. Table 1 lists As L_3-edge absorption energies for various *M*As and $MAs_{1-y}P_y$ compounds, and Fig. 4c shows a plot of these energies vs difference in electronegativity ($\Delta\chi = \chi_{As} - \chi_M$). Like the P energies in *M*P (Fig. 4a and b), the As L_3-edge absorption energies decrease linearly in the binary arsenides *M*As through the series from CoAs to VAs. The As L_3-edge absorption energies in the mixed pnictides $MAs_{1-y}P_y$ deviate from this linear trend and, opposite to the behaviour of the P energies, they are *higher* than expected, with deviations that increase with the increase in P concentration in a given $MAs_{1-y}P_y$ series.

The As K-edge absorption spectra are more complex. Representative spectra for FeAs and some $FeAs_{1-y}P_y$ members collected in transmission mode are shown in Fig. 6a. On the basis of previous studies on other As-containing compounds, the low-energy white-line intensity (labelled A) is assigned to be a pre-edge peak [28]. By comparison of the spectra to the calculated conduction states (Fig. 6b), this peak can be ascribed to a dipolar transition in which As 1*s* electrons are excited into bound As 4*p* states located below the continuum states (absorption threshold). Because As 4*p* states are involved in bonding, the intensity of this pre-edge peak can provide information on charge. This peak intensifies going from FeAs to $FeAs_{0.10}P_{0.90}$, implying that the As charge becomes less negative (more neutral) with increasing *y* (greater P concentration) in $FeAs_{1-y}P_y$. This trend is also observed in the $CoAs_{1-y}P_y$ and $CrAs_{1-y}P_y$ series. Moreover, this pre-edge peak becomes less intense through the sequence CoAs, FeAs, and CrAs, consistent with the decrease in As L_3-edge energy seen earlier in Fig. 4c. In general, pre-edge intensities are quite sensitive to charge, as has been shown in studies of the Au L_3-edge in a series of compounds where an increase in charge from 0 to 1+ causes the pre-edge peak to intensify by as much as ~40% [29]. Likewise, the As charge does not have to change much to produce substantial changes in the pre-edge peak intensity. Peak A is much less intense in *M*As and $MAs_{1-y}P_y$ (Fig. 6a), where the As charge is near 1−, than in As_2S_3, where the As charge is nominally 3+ [28]. (The P K-edge spectra could not be analysed similarly because they were collected in fluorescence mode, where self-absorption effects in thick samples may appreciably affect peak intensities [30].)

Two higher-energy resonances (labelled B and C) are also present in Fig. 6a. By comparison to the calculated conduction

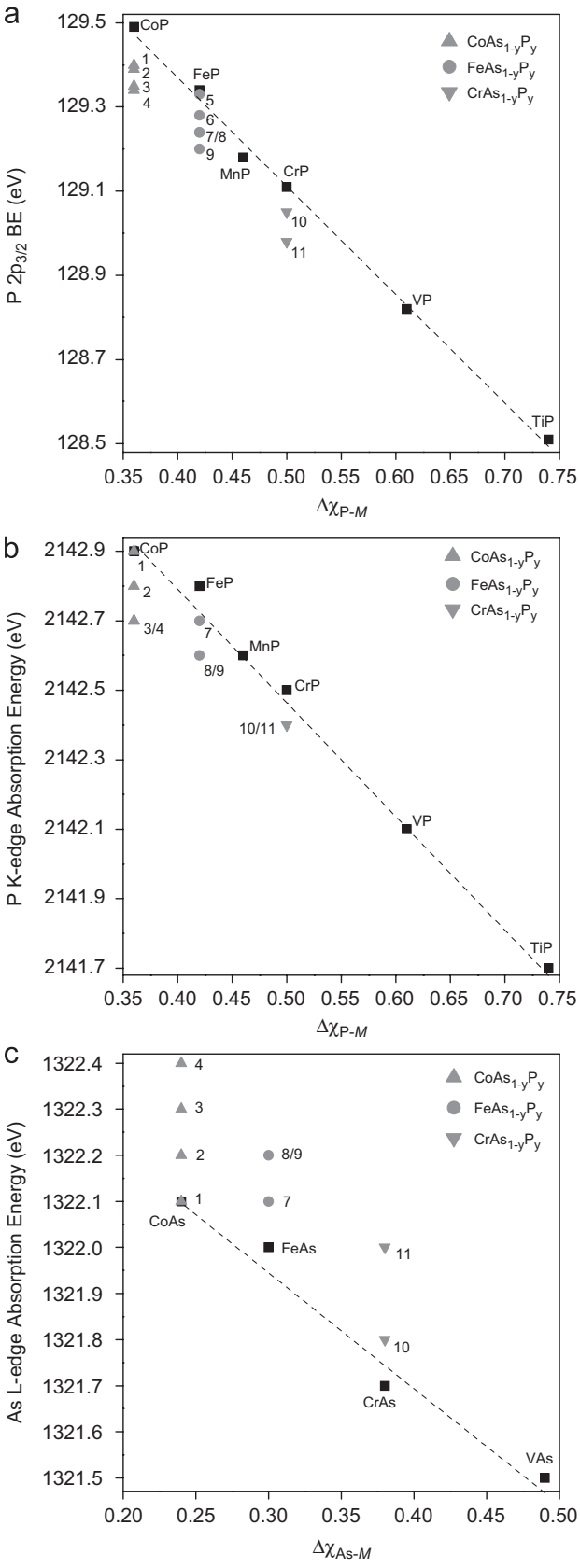

Fig. 4. Dependence of: (a) P $2p_{3/2}$ BE, (b) P K-edge absorption energy, and (c) As L_3-edge absorption energy on electronegativity difference ($\Delta\chi = \chi_{Pn} - \chi_M$) for binary pnictides *M*P or *M*As (■) and ternary mixed pnictides $CoAs_{1-y}P_y$ (▲) (1 = $CoAs_{0.75}P_{0.25}$, 2 = $CoAs_{0.50}P_{0.50}$, 3 = $CoAs_{0.25}P_{0.75}$, 4 = $CoAs_{0.10}P_{0.90}$), $FeAs_{1-y}P_y$ (●) (5 = $FeAs_{0.90}P_{0.10}$, 6 = $FeAs_{0.75}P_{0.25}$, 7 = $FeAs_{0.50}P_{0.50}$, 8 = $FeAs_{0.25}P_{0.75}$, 9 = $FeAs_{0.20}P_{0.90}$), and $CrAs_{1-y}P_y$ (▼) (10 = $CrAs_{0.75}P_{0.25}$, 11 = $CrAs_{0.10}P_{0.90}$). The *M*P P $2p_{3/2}$ BEs and P K-edge absorption energies are from Refs. [11,12].

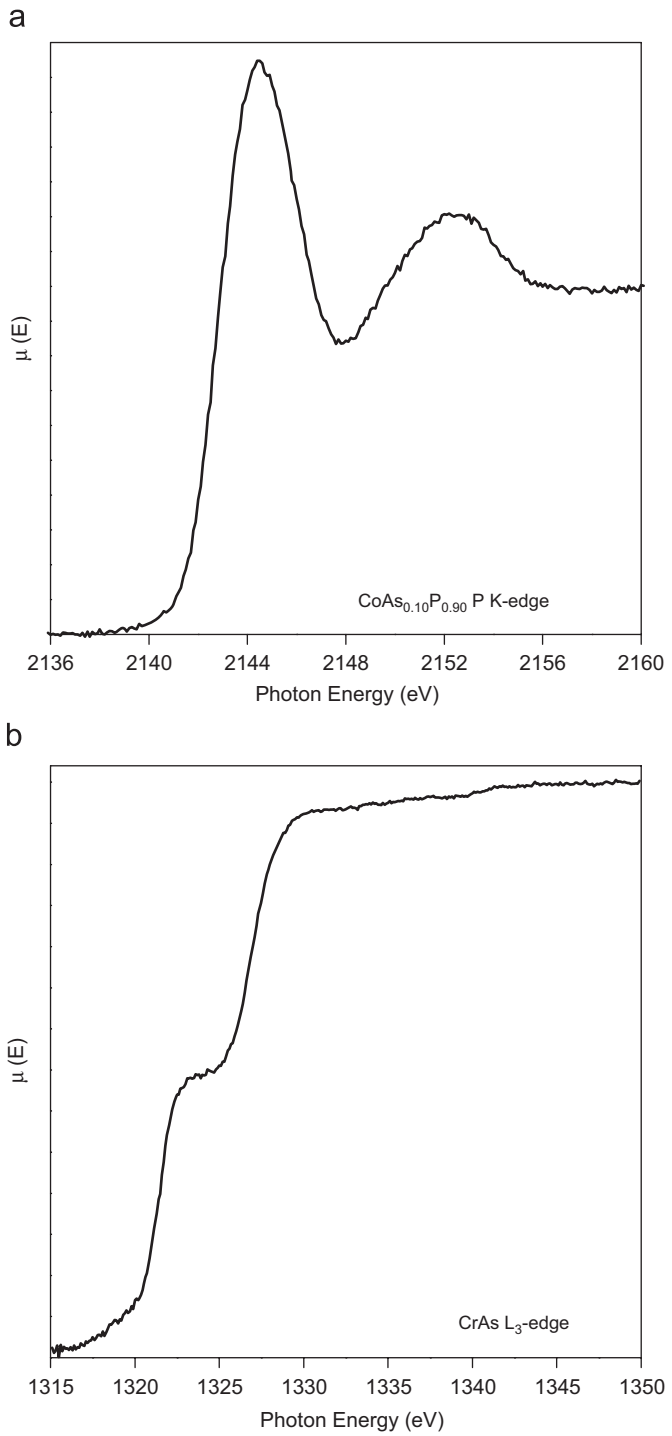

Fig. 5. (a) P K-edge XANES spectrum for $CoAs_{0.10}P_{0.90}$ and (b) As L_3-edge XANES spectrum for CrAs. All spectra were measured in fluorescence mode.

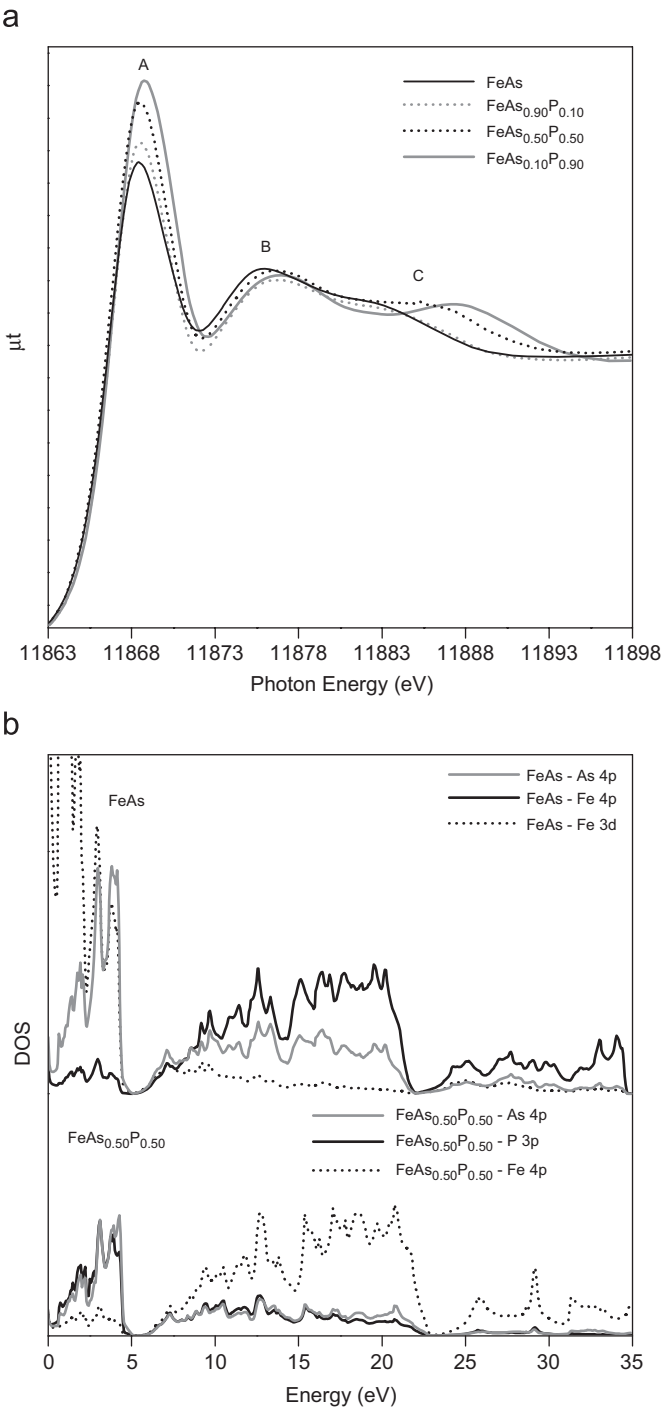

Fig. 6. (a) Normalized As K-edge absorption spectra, collected in transmission mode, for FeAs and some $FeAs_{1-y}P_y$ compounds. Identification of peaks A–C is discussed in the text. (b) Orbital projections of the calculated conduction states of FeAs and $FeAs_{0.50}P_{0.50}$. The Fermi edge (E_F) is at 0 eV.

states (Fig. 6b), they may be initially assigned as excitations from As 1*s* to As 4*p*, P 3*p*, or Fe 4*p* states. However, these peaks resemble those found in the As K-edge spectrum of As_2S_3, where they are attributed to EXAFS phenomena [28]. This alternative interpretation is supported by the observation that peaks B and C shift to higher energy with greater *y* in $FeAs_{1-y}P_y$ (Fig. 6a), consistent with the expectation that the energy is inversely proportional to the scattering path length [31] and that the average Fe–*Pn* bond distance shortens as the P concentration increases. The presence of a strong pre-edge peak (A) and intense EXAFS peaks (B and C) makes it difficult to track variations in the threshold energy, which is buried beneath these features. Nevertheless, there does appear to be a trend in the As K-edge energies (Table 1). Similar to the As L_3-edge absorption energies, the As K-edge energies decrease going from CoAs to CrAs. The absorption energies for the $MAs_{1-y}P_y$ compounds are, in general, higher than those observed for *M*As and increase with increasing *y*. For example, in the $FeAs_{1-y}P_y$ series, the As K-edge absorption energies are 11866.6 eV for FeAs to $FeAs_{0.50}P_{0.50}$, and increase to 11866.8 eV for $FeAs_{0.25}P_{0.75}$ and to 11866.9 eV for

$FeAs_{0.10}P_{0.90}$. This agrees well with the trend in As L_3-edge energies (Fig. 4c, Table 1).

3.4. M 2p XPS spectra

Fig. 7 shows *M* 2*p* XPS spectra for a representative member of each $MAs_{1-y}P_y$ (M = Cr, Fe, Co) series and for the parent binary pnictides *M*P and *M*As. Table 1 lists the *M* $2p_{3/2}$ BEs. All spectra exhibit an asymmetric lineshape, which is characteristic of an itinerant electronic structure, as first described by Doniach and Šunjić [32]. This type of lineshape arises when valence electrons, interacting with the core hole (produced by photoionization), are excited and scattered from filled states below the Fermi edge to empty conduction states above. Because there is a continuum of states above the Fermi edge in metallic compounds such as those investigated here, an asymmetric tail comprising many closely spaced states is observed instead of a few distinct satellite peaks [33]. As in the binary and mixed-metal phosphides *M*P and $M_{1-x}M'_xP$ investigated previously [11,12], this lineshape originates from the electronic delocalization associated with the metal–metal bonding network found in the MnP-type structure also adopted by *M*As and $MAs_{1-y}P_y$.

Through the series from *M*P to *M*As, the *M* $2p_{3/2}$ BE decreases slightly for M = Fe and Co, but hardly changes for M = Cr (Fig. 7 and Table 1), when the precision of $\sim\pm0.10$ eV is taken into consideration. The smaller BE in the metal arsenides *M*As is consistent with the less positive *M* charge resulting from the presence of less electronegative As atoms and more covalent *M*–As bonds. The absence of a shift on going from CrP to CrAs probably reflects the diminishing magnitude of the relative electronegativity differences as *M* becomes less electronegative (cf., $\Delta\chi_{Cr-P}/\Delta\chi_{Cr-As} = 1.3$ vs $\Delta\chi_{Co-P}/\Delta\chi_{Co-As} = 1.5$) [26].

The Co $2p_{3/2}$ spectra also exhibit a high BE satellite (Fig. 7c), which has been previously attributed to plasmon loss [11,12,27], in which the kinetic energy of the photoelectron is reduced because of oscillations of bound valence electrons, leading to an apparent increase in BE [34]. This interpretation has been corroborated by identifying the occurrence of the same phenomenon in most of the first-row transition metals (Sc–Ni) [35–39]. Note that no such plasmon loss peak is observed in the Fe or Cr $2p_{3/2}$ spectra, likely because it is overlapped by the much more intense core line. The plasmon loss peak weakens as Co becomes more positively charged, as seen in the Co $2p_{3/2}$ spectra for the series $Co^{x+}P_x$ (x = 0, 1, 3); this observation implies that the cross-section for producing a plasmon oscillation decreases as the Co 3*d* valence orbitals are depleted of electron density [27]. The plasmon loss peak may also become less intense as the number of spin-unpaired electrons decreases, as observed in the 1*s* XPS spectra of Sc–Co measured with a Cu $K\alpha$ X-ray source [39]. Fig. 8 shows a plot of the Co $2p_{3/2}$ plasmon loss intensity (normalized to the core-line intensity) vs y for the $CoAs_{1-y}P_y$ series. As the P concentration (y) increases, the intensity of the plasmon loss peak diminishes, implying that Co becomes more positively charged as we progress from CoAs to CoP.

3.5. M L- and K-edge XANES spectra

Further insight on the charges of *M* atoms in $MAs_{1-y}P_y$ can be provided by the *M* L- and K-edge XANES spectra. In the L-edge spectra, *M* 2*p* electrons are promoted into unoccupied *M* 3*d* and possibly *M* 4*s* states, so the intensity of the L_3 and L_2 peaks reveals information about the *M* charge. Fig. 9 shows normalized Fe L-edge spectra for representative members of the $FeAs_{1-y}P_y$ series. The two resolved L_3 peaks can be assigned to the 3*d* t_{2g} and e_g

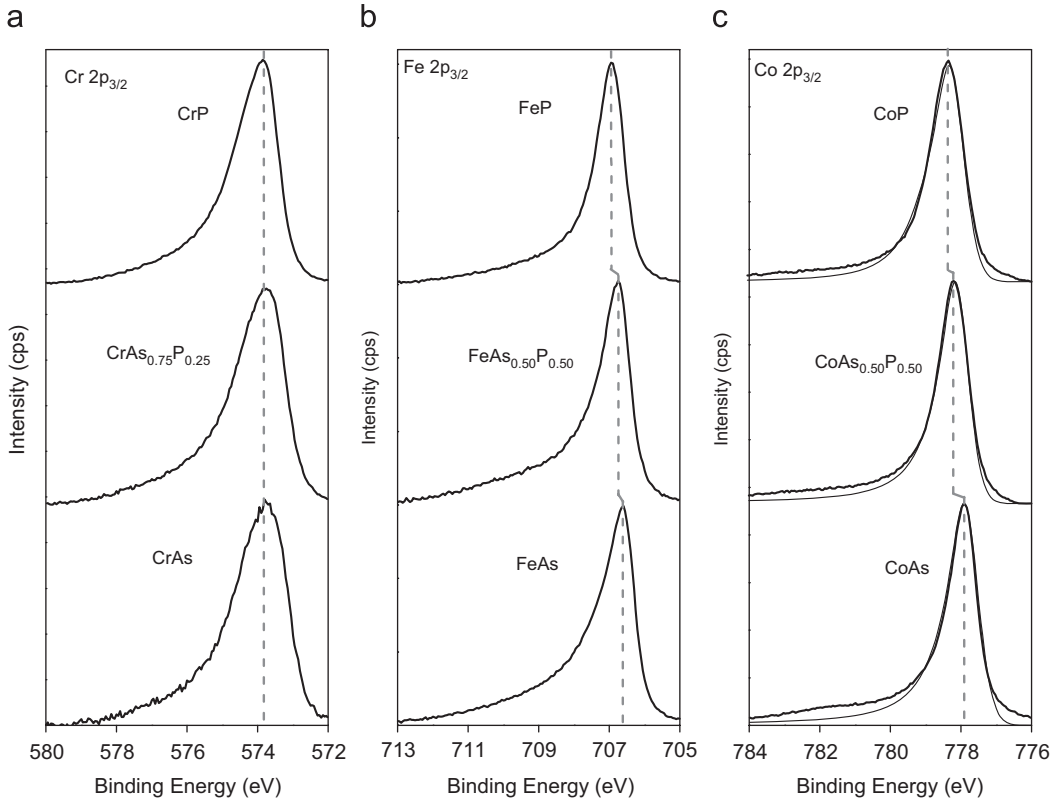

Fig. 7. Representative metal $2p_{3/2}$ XPS spectra for (a) $CrAs_{1-y}P_y$, (b) $FeAs_{1-y}P_y$, and (c) $CoAs_{1-y}P_y$, compared to the parent binary phosphides and arsenides. The spectra for CrP, FeP, and CoP are from Ref. [11]. The Co $2p_{3/2}$ spectra were fitted with an asymmetric peak (thin solid line), revealing the superimposed high-BE satellite peak. The $2p_{3/2}$ BEs, which are listed in Table 1, are marked by vertical dashed lines.

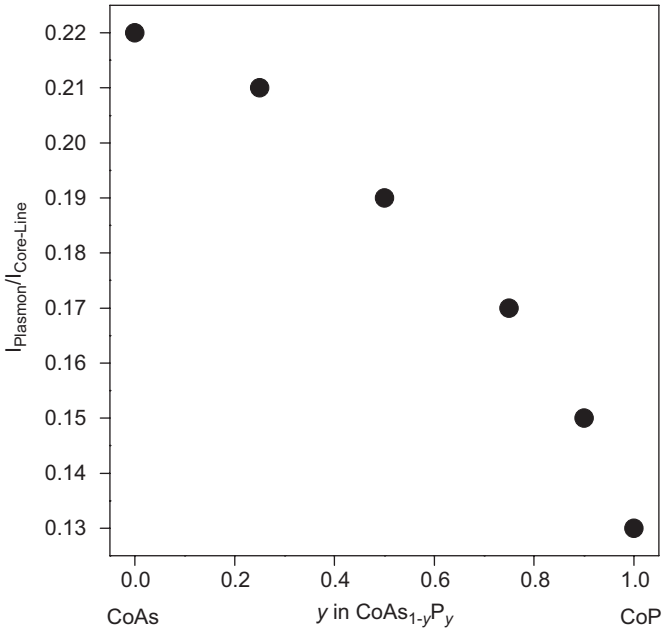

Fig. 8. Plot showing the variation in the normalized plasmon intensity vs y in the Co 2p spectra for $CoAs_{1-y}P_y$. The value for CoP is from Ref. [27].

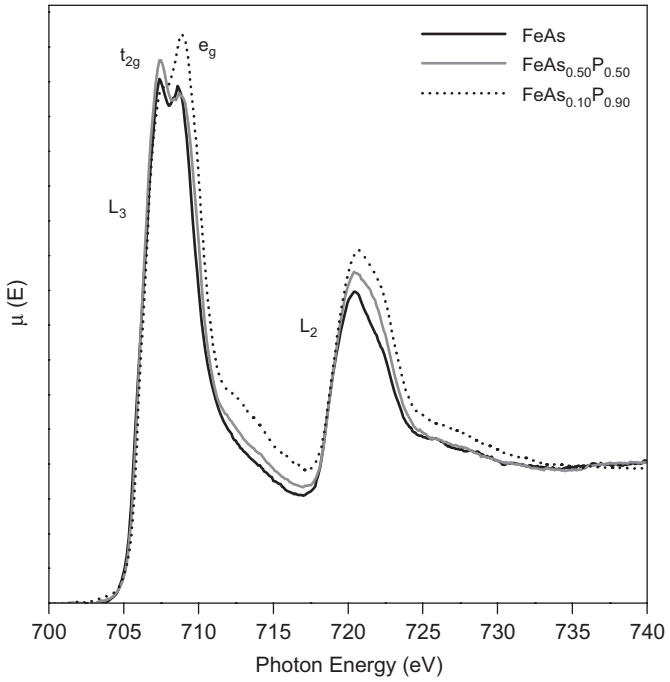

Fig. 9. Normalized total electron yield Fe $L_{2,3}$-edge XANES spectra for FeAs and some $FeAs_{1-y}P_y$ compounds. The small shoulders observed just above the L_3 and L_2 edges in the $FeAs_{0.10}P_{0.90}$ spectrum probably arise from some surface oxide formed.

states of the Fe atoms, which are surrounded by pnicogen atoms in a distorted octahedral coordination. The L_2 peak is not resolved into distinct t_{2g} and e_g states because of spectral broadening resulting from a decreased lifetime of the final state. Both L_3 and L_2 peaks are more intense in $FeAs_{0.10}P_{0.90}$ and $FeAs_{0.50}P_{0.50}$ than in FeAs; in particular, the e_g portion of the L_3 peak is considerably enhanced in $FeAs_{0.10}P_{0.90}$. These intensity changes imply that the 3d states are depopulated and thus the Fe charge becomes more positive as y increases in $FeAs_{1-y}P_y$. Similar results were obtained for the $CoAs_{1-y}P_y$ series, whereas difficulties in normalizing the spectra made such an analysis impossible for the $CrAs_{1-y}P_y$ series.

Cr K-edge spectra for the $CrAs_{1-y}P_y$ series (including the end-members CrP and CrAs) are shown in Fig. 10. The lineshape for the spectrum of CrP is very similar to that observed in the Mn K-edge spectrum of MnP [12,40]. The spectra contain three main excitations, labelled A, B, and C. Peak A is a pre-edge peak in which Cr 1s electrons are primarily excited into unoccupied Cr 3d states, or possibly also into Cr 4p and *Pn* np states, from inspection of the calculated conduction states for CrAs, which resemble those for FeAs (Fig. 6b). These states overlap near the Fermi edge because the distorted octahedral coordination around Cr atoms entails some participation of Cr 4p orbitals in bonding [41]. Peak A (Cr 1s→Cr 3d) is a quadrupolar transition and therefore it is much weaker than peaks B (Cr 1s→*Pn* np) and C (Cr 1s→Cr 4p), which are dipolar transitions. Similar transitions have been identified in the Mn K-edge spectrum of MnP [40]. As in the argument pertaining to the M L-edge spectra above, the intensity of the pre-edge peak here reveals information about the M charge (when the coordination environment of M is fixed). The pre-edge peak intensifies on proceeding from CrAs, through $CrAs_{1-y}P_y$, to CrP (inset of Fig. 10), indicating that the 3d states are gradually depopulated and the Cr charge becomes more positive as y increases in $CrAs_{1-y}P_y$. Also apparent from Fig. 10, the Cr K-edges gradually shift to higher energy as we progress from CrAs to CrP, consistent with an increase in Cr charge. Although the energy shift of peak C (which affects the apparent intensity of peak B) may be traced to the increase in energy of the M 4p states on going from MAs through $MAs_{1-y}P_y$ (Fig. 6b), it can also be explained by a shift

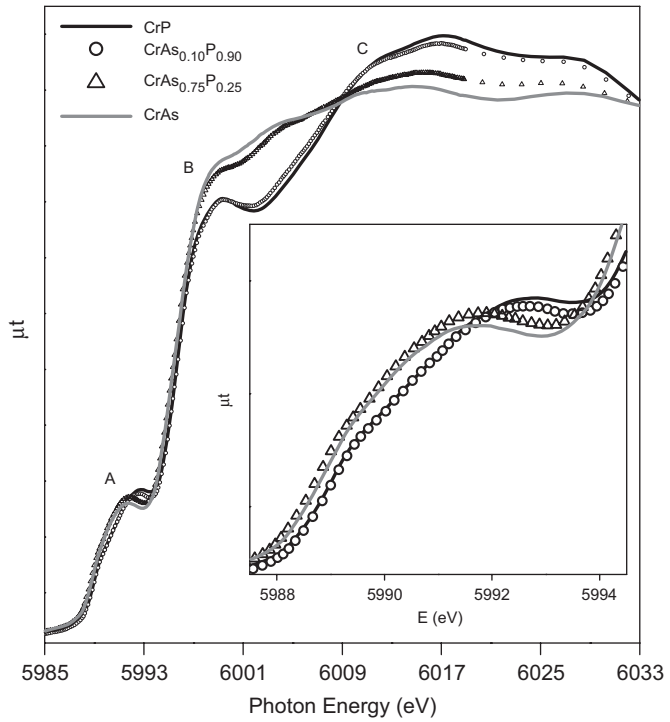

Fig. 10. Normalized Cr K-edge XANES spectra, collected in transmission mode, for $CrAs_{1-y}P_y$. Peak A primarily represents a pre-edge Cr 1s→Cr 3d transition. Based on comparison to the calculated conduction states of FeAs and $FeAs_{0.50}P_{0.50}$ (Fig. 6b), peak B may represent a Cr 1s→*Pn* np transition whereas peak C may represent a Cr 1s→Cr 4p transition or an EXAFS feature (see text). The inset highlights the differences in pre-edge peak intensity among the four compounds.

of the EXAFS, as proposed in the discussion of the As K-edge spectra (Section 3.3). Analysis of the $FeAs_{1-y}P_y$ and $CoAs_{1-y}P_y$ K-edge spectra gave similar conclusions to those above.

4. Discussion

4.1. Shifts in P $2p_{3/2}$ BE and P K-edge absorption energies

The trend in P $2p_{3/2}$ BE within a given $MAs_{1-y}P_y$ series is unusual: the BE gradually decreases as the $MAs_{1-y}P_y$ series becomes more phosphorus rich (higher y) but the BE abruptly increases when the end-member binary phosphide MP itself is reached (Table 1 and Fig. 4a). Relaxation effects may be considered first. Previous investigations in gas-phase molecules have shown that, as long as the coordination geometry is retained, substitution of more *electropositive* atoms in the coordination environment enhances relaxation towards the nucleus of the central atom under study, lowering its BE [42]. In the $MAs_{1-y}P_y$ series, a central P atom is surrounded by M atoms in the first coordination sphere and pnicogen (P or As) atoms in the second coordination sphere. Substitution of more *electronegative* P atoms in the coordination environment lowers the BE of the central P atom, opposite to expectations and an observation that rules out significant relaxation effects. Moreover, the trend in P K-edge absorption energies (Fig. 4b) is consistent with the trend shown by phosphorus BEs. Absorption energies are less influenced by relaxation effects than are BEs, because of the greater screening that is maintained in the absorption process. An estimate of the ability of electrons to screen the nuclear charge can be made from the values of Z_{eff}, which can be calculated with Slater's rules [43]. A neutral P atom yields a Z_{eff} value of 4.45, a photoionized P atom with a 1s core hole (i.e., P^{1+}) has a value of 5.45, and for the photo-absorption process, which can be modelled by promotion of a 1s electron into an empty 3p orbital (P^*), a value of 5.10 is determined [43]. The nuclear charge is thus better screened in P^* than in P^{1+}, implying that relaxation of electrons towards the nucleus will be less important in the absorption process compared to the photoemission process. The trends in P BEs and absorption energies (Fig. 4a and b) are thus attributed to ground-state effects as described by the charge potential model (Eq. 1). Because these energy shifts are close to the limit of precision of the measurements, we offer only a qualitative analysis below.

The charges on M and As that are formed within a given $MAs_{1-y}P_y$ series can be deduced. As y increases, the As atoms become less negatively charged (from As K-edge spectra (Section 3.3)), not only because they give up electron density to the more electronegative P atoms via the weak *Pn–Pn* bonding network, but also because they are less capable than the P atoms in competing for electron density donated by the M atoms. As y increases, the M atoms also become more positively charged (as derived from Co plasmon loss peak intensities (Section 3.4) and Fe $L_{2,3}$-edge and Cr K-edge spectra (Section 3.5)), because the *M–Pn* bond becomes more ionic, on average. Applying the constraints that (i) the average *Pn* charge balances the M charge in $MAs_{1-y}P_y$ (i.e., a concentration factor must be included) and (ii) the P charge in MP is more negative than the As charge in MAs, in agreement with relative electronegativities, we can deduce that the P atoms become less negatively charged as y increases in $MAs_{1-y}P_y$ (Fig. 11). A physical interpretation of this trend is that as P atoms gradually substitute for As atoms in a $MAs_{1-y}P_y$ series, the required total negative charge can be distributed over a greater number of the more electronegative P atoms, such that each P atom, on average, does not need to carry as high a negative charge.

According to Eq. (1), the P $2p_{3/2}$ BE and P K-edge absorption energies should both increase with increasing proportion of P atoms as we proceed from $MAs_{1-y}P_y$ ($y<1$) to MP, because q_i becomes less negative (in $k\Delta q_i$) and the Madelung potential ($\Delta\Sigma_{j\neq i}\, q_j/r_{ij}$) becomes more positive, if only the first coordination shell containing the M atoms is considered. For very P-rich members (high y), however, the second coordination shell now contains many P atoms, which provide better screening to the photoemission or absorption site than the As atoms because they are more electronegative (more negative q_j values) and they are closer (smaller r_{ij} distances). Thus, next-nearest neighbour (interatomic) effects can become quite important in overcoming and reversing trends controlled by the atomic charge alone. In this present series, the P $2p$ BE and P K-edge absorption energy values actually become lower as y increases in $MAs_{1-y}P_y$ ($0<y<1$), with an abrupt increase in the P $2p$ BE and K-edge absorption energy being observed for the pure MP end member. This jump can be related to the reduced screening of the P photoemission or absorption site provided by the less negatively charged P atoms and the more positively charged M atoms present in the pure end members compared to the values found in the mixed $MAs_{1-y}P_y$ series.

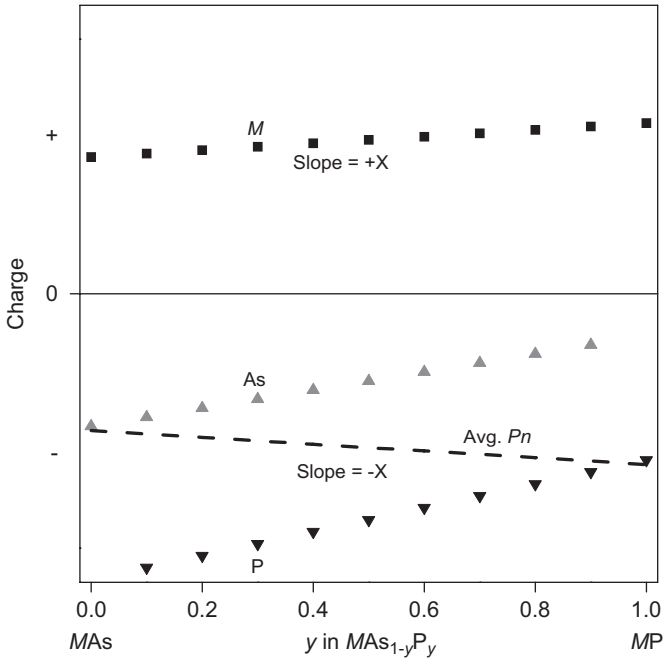

Fig. 11. Schematic representation of the dependence of M (■) and *Pn* (P, ▼; As, ▲) charges on y in $MAs_{1-y}P_y$. The average *Pn* charge ($q_{Pn} = yq_P+(1-y)q_{As}$), represented by the dashed line, balances the M charge in $MAs_{1-y}P_y$.

4.2. Shifts in As L_3- and K-edge absorption energies

In the binary arsenides MAs, the As L_3- and K-edge absorption energies decrease as the difference in electronegativity ($\Delta\chi = \chi_{As}-\chi_M$) increases, consistent with the development of more negatively charged As atoms as the *M–*As bond becomes more ionic and consistent with a more negative $k\Delta q_i$ term in Eq. (1). This trend is confirmed by the attenuation of the pre-edge peak in the As K-edge spectra through the series from CoAs to CrAs (Section 3.3).

In the mixed pnictides $MAs_{1-y}P_y$, the As L_3- and K-edge absorption energies increase with y, opposite to the trend shown by the P energies. This occurs not only because the As atoms become less negatively charged (less negative $k\Delta q_i$ term), but also because the M atoms in the first coordination shell become more positively charged (more positive $\Delta\Sigma_{j\neq i}\, q_j/r_{ij}$ term). The next-nearest neighbour effects associated with the *Pn* atoms in the second coordination shell will not be as important because they are further away from the larger As atom.

5. Conclusions

Binary phosphides (*M*P) and arsenides (*M*As) show a linear decrease in the P or As BEs and absorption energies with greater difference in electronegativity ($\Delta\chi = \chi_{Pn} - \chi_M$) because the pnicogen atoms become more negatively charged as the ionic character in the *M*–*Pn* bond increases. However, mixed arsenide phosphides $MAs_{1-y}P_y$ with the MnP-type structure do not show this behaviour. As *y* increases, the P $2p_{3/2}$ XPS BEs and P K-edge absorption energies decrease and are always lower than those for the binary phosphides *M*P, whereas the As L_3- and K-edge absorption energies increase and are always higher than those for the binary arsenides *M*As. These trends can be rationalized within the charge potential model, taking into consideration the contribution of next-nearest neighbour effects arising from the presence of a *Pn*–*Pn* bonding network and the competition between the two different anions for electron density from the more electropositive *M* atoms.

With increasing *y*, the As atoms become less negatively charged in $MAs_{1-y}P_y$ than in *M*As, consistent with an observed increase in the As L_3- and K-edge absorption energy. The P atoms are more negatively charged in $MAs_{1-y}P_y$ than in *M*P, consistent with observed decreases in the P $2p_{3/2}$ BE and P K-edge absorption energy. Lastly, the *M* atoms become more positively charged with increasing *y* in $MAs_{1-y}P_y$, consistent with the Co 2*p* XPS spectra and the *M* L- and K-edge absorption spectra. Importantly, the metal atoms in the first coordination shell and the pnicogen atoms in the second coordination shell modify the Madelung potential operating on the pnicogen centres and thus affect their BE and absorption energies (particularly for P) indicating the importance of near and next-nearest neighbour effects on these energies. The variation of the *M*, As, and P charges in the $MAs_{1-y}P_y$ series reflects a considerable tunability in the electronic structure of MnP-type compounds, which could prove useful in catalytic applications.

Acknowledgments

The Natural Sciences and Engineering Research Council (NSERC) of Canada supported this work through Discovery Grants to R.G.C. and A.M. Access to the Kratos XPS was kindly provided by the Alberta Centre for Surface Engineering and Science (ACSES) at the University of Alberta. ACSES was established with capital funding from the Canada Foundation for Innovation (CFI) and Alberta Innovation and Science. CFI also provides interim operating support. Dr. Robert Blyth and Dr. J. Thompson of the Canadian Light Source (CLS) are thanked for help in carrying out the *M* L-, As L-, and P K-edge XANES measurements at 11-ID.1 at the CLS. The CLS is supported by NSERC, NRC, CIHR, and the University of Saskatchewan. Dr. Robert Gordon of PNC-XOR is thanked for help in carrying out the *M* K-, and As K-edge XANES experiments at PNC/XOR-CAT, sector 20 at the APS. PNC/XOR facilities at the Advanced Photon Source (APS), and research at these facilities, are supported by the US Department of Energy-Basic Energy Sciences, a major research support grant (MRS) from NSERC, the University of Washington, Simon Fraser University, and the APS. Use of the APS is also supported by the US Department of Energy, Office of Science, Office of Basic Energy Sciences, under Contract DE-AC02-06CH11357. A.P.G. thanks NSERC, Alberta Ingenuity and the University of Alberta for support.

Appendix A. Supplementary data

Supplementary data associated with this article can be found in the online version at doi:10.1016/j.jssc.2008.06.034.

References

[1] P.A.W. van der Heide, Surf. Sci. 490 (2001) L619–L626.
[2] P.A.W. van der Heide, J. Electron Spectrosc. Relat. Phenom. 151 (2006) 79–91.
[3] A.R. Gerson, T. Bredow, Surf. Interface Anal. 29 (2000) 145–150.
[4] K. Siegbahn, C. Nordling, A. Fahlman, R. Nordberg, K. Hamrin, J. Hedman, G. Johansson, T. Bergmark, S.-E. Karlsson, I. Lindgren, B. Lindberg, ESCA: Atomic, Molecular and Solid State Structure Studied by Means of Electron Spectroscopy, Almqvist and Wiksells Boktryckeri AB, Uppsala, 1967.
[5] D.T. Clark, D. Kilcast, J. Chem. Soc. B: Phys. Org. Chem. (1971) 2243–2247.
[6] D. Briggs, Surface Analysis of Polymers by XPS and Static SIMS, Cambridge University Press, Cambridge, 1998.
[7] J.J. Rehr, R.C. Albers, Rev. Mod. Phys. 72 (2000) 621–654.
[8] J. Wong, F.W. Lytle, R.P. Messmer, D.H. Maylotte, Phys. Rev. B 30 (1984) 5596–5610.
[9] A.H. de Vries, L. Hozoi, R. Broer, Int. J. Quantum Chem. 91 (2003) 57–61.
[10] A. Mottana, A. Marcelli, G. Biuli, Z. Wu, F. Seifert, E. Paris, Phys. Chem. Miner. 23 (1996) 227–228.
[11] A.P. Grosvenor, S.D. Wik, R.G. Cavell, A. Mar, Inorg. Chem. 44 (2005) 8988–8998.
[12] A.P. Grosvenor, R.G. Cavell, A. Mar, J. Solid State Chem. 180 (2007) 2702–2712.
[13] H. Fjellvåg, A. Kjekshus, A. Zieba, S. Foner, J. Phys. Chem. Solids 45 (1984) 709–718.
[14] S.T. Oyama, J. Catal. 216 (2003) 343–352.
[15] S. Rundqvist, P.C. Nawapong, Acta Chem. Scand. 19 (1965) 1006–1008.
[16] K. Selte, A. Kjekshus, T.A. Oftedal, A.F. Andresen, Acta Chem. Scand. A 28 (1974) 957–962.
[17] K. Kanaya, S. Abe, H. Yoshida, K. Kamigaki, T. Kaneko, J. Alloys Compd. 383 (2004) 189–194.
[18] A.R. Denton, N.W. Ashcroft, Phys. Rev. A 43 (1991) 3161–3164.
[19] N. Fairley, CasaXPS, version 2.3.9, Casa Software Ltd., Teighnmouth, Devon, UK, 2003 〈www.casaxps.com〉.
[20] T. Regier, J. Paulsen, F. Wright, I. Coulthard, K. Tan, T.K. Sham, R.I.R. Blyth, AIP Conf. Proc. 879 (2007) 473–476.
[21] C. Engemann, G. Kohring, A. Pantelouris, J. Hormes, S. Grimme, S.D. Peyerimhoff, J. Clade, F. Frick, M. Jansen, Chem. Phys. 221 (1997) 189–198.
[22] B. Ravel, M. Newville, J. Synchrotron Radiat. 12 (2005) 537–541.
[23] O.K. Andersen, Phys. Rev. B 12 (1975) 3060–3083.
[24] J.E. Huheey, E.A. Keiter, R.L. Keiter, Inorganic Chemistry: Principles of Structure and Reactivity, 4th ed, Harper Collins, New York, 1993.
[25] L. Pauling, The Nature of the Chemical Bond, 3rd ed, Cornell University Press, Ithaca, NY, 1960.
[26] A.L. Allred, E.G. Rochow, J. Inorg. Nucl. Chem. 5 (1958) 264–268.
[27] A.P. Grosvenor, R.G. Cavell, A. Mar, Phys. Rev. B 74 (2006), 125102/1–125102/10.
[28] G. Pfeiffer, J.J. Rehr, D.E. Sayers, Phys. Rev. B 51 (1995) 804–810.
[29] A. Pantelouris, G. Kuper, J. Hormes, C. Feldmann, M. Jansen, J. Am. Chem. Soc. 117 (1995) 11749–11753.
[30] I. Arcon, J. Kolar, A. Kodre, D. Hanzel, M. Strlic, X-ray Spectrom. 36 (2007) 199–205.
[31] M.E. Fleet, Can. Miner. 43 (2005) 1811–1838.
[32] S. Doniach, M. Šunjić, J. Phys. C: Solid State Phys. 3 (1970) 285–291.
[33] S. Hüfner, in: L. Ley, M. Cardona (Eds.), Photoemission in Solids II, Spinger, Berlin, 1979.
[34] R.F. Egerton, M. Malac, J. Electron Spectrosc. Relat. Phenom. 143 (2005) 43–50.
[35] H.A.E. Hagelin-Weaver, G.B. Hoflund, D.M. Minahan, G.N. Salaita, Appl. Surf. Sci. 235 (2004) 420–448.
[36] H.A.E. Hagelin-Weaver, J.F. Weaver, G.B. Hoflund, G.N. Salaita, J. Alloys Compd. 389 (2005) 34–41.
[37] A.P. Grosvenor, M.C. Biesinger, R.S.-C. Smart, N.S. McIntyre, Surf. Sci. 600 (2006) 1771–1779.
[38] N. Moslemzadeh, G. Beamson, P. Tsakiropoulos, J.F. Watts, Surf. Sci. 600 (2006) 265–277.
[39] N. Moslemzadeh, G. Beamson, P. Tsakiropoulos, J.F. Watts, S.R. Haines, P. Weightman, J. Electron Spectrosc. Relat. Phenom. 152 (2006) 129–133.
[40] F.M.F. de Groot, S. Pizzini, A. Fontaine, K. Hämäläinen, C.C. Kao, J.B. Hastins, Phys. Rev. B 51 (1995) 1045–1050.
[41] P.G. Perkins, A.K. Marwaha, J.J.P. Stewart, Theor. Chim. Acta 59 (1981) 569–583.
[42] R.G. Cavell, R.N.S. Sodhi, J. Electron Spectrosc. Relat. Phenom. 41 (1986) 23–35.
[43] J.C. Slater, Phys. Rev. 36 (1930) 57–64.